Optimal Three-Dimensional Current Computation Flux Weakening Control Strategy for DC-Biased Vernier Reluctance Machines Considering Inductance Nonlinearity

Zixiang Yu, *Student Member, IEEE*, Wubin Kong, *Member, IEEE*, Ronghai Qu, *Fellow, IEEE*, Dawei Li, *Member, IEEE*, Shaofeng Jia, *Member, IEEE*, Dong Jiang, *Senior Member, IEEE*, Jianbo Sun, *Member, IEEE*, and Hongtao Li

***Abstract*—An optimal three-dimensional current computation flux weakening control strategy for dc-biased Vernier reluctance machines (VRMs) is proposed in this paper. Compared with permanent magnet synchronous machines, dc-biased VRMs have an additional degree of freedom to regulate the rotor flux through variable dc-biased armature current. The conventional flux weakening control strategy does not utilize the adjustable dc field current, and the output capacity in the flux weakening region is limited. In this paper, the optimal three-dimensional current distribution is calculated at the intersection of current and voltage constraint. Meanwhile, in order to maintain the armature voltage within the voltage constraint, the inductance nonlinearity is reflected by constructing the inductance table. The algorithm provides maximum output capability and high efficiency for dc-biased VRMs despite the changes in inductance parameters in the whole flux weakening region. Finally, the effectiveness of the proposed control strategy is validated by experimental results for a prototype machine.**

***Index Terms*—DC-biased, control strategy, flux weakening, inductance nonlinearity, three-dimensional current, Vernier reluctance machine (VRM).**

Manuscript received October 21, 2017; revised January 2, 2018 and March 5, 2018; accepted April 20, 2018. Date of publication April 29, 2018; date of current version December 7, 2018. This work was supported by the National Natural Science Foundation of China under Project 51607078, 51607079, and 51520105010, and the National Key Research and Development Program of China under project 2017YFB0102300 and 2017YFB0102400. Recommended for publication by Associate Editor B. G. Fernandes. *(Corresponding author: Wubin Kong.)*

Z. Yu, W. Kong, R. Qu, D. Li, D. Jiang, and J. Sun are with the State Key Laboratory of Advanced Electromagnetic Engineering and Technology, School of Electrical and Electronic Engineering, Huazhong University of Science and Technology, Wuhan 430074, China (e-mail: yuzixiang@hust.edu.cn; wubinkong@126.com; ronghaiqu@hust.edu.cn; daweili@hust.edu.cn; jiangd@hust.edu.cn; jianbo.sun@hust.edu.cn).

S. Jia is with the School of Electrical Engineering, Xi'an Jiaotong University, Xi'an 710049, China (e-mail: d201277318@hust.edu.cn).

H. Li is with the State Grid Zhejiang Electric Power Company Hangzhou Power Supply Company, Hangzhou 310000, China (e-mail: 517194614@qq.com).

Color versions of one or more of the figures in this paper are available online at http://ieeexplore.ieee.org.

Digital Object Identifier 10.1109/TPEL.2018.2831248

I. Introduction

PERMANENT magnet synchronous machines (PMSMs) exhibit high torque density, high-power factor, and high efficiency merits [1]–[4]. However, the high permanent magnet (PM) material cost limits the competitiveness of PMSMs in certain low-cost applications. Meanwhile, flux weakening control is required in most of the traction applications using PMSMs, the uncontrollable PM flux-linkage limits the flux weakening capability.

To achieve wide operation range, it is possible to use traditional rotor wound field synchronous machines (RWFSMs) [5]–[8]. The rotor current is utilized as an additional degree of freedom, and it allows high achievable system efficiency in all operation ranges. However, in these conventional RWFSMs, brushes and slip rings are usually required in order to supply the dc current to the rotor, which has restricted their potential in wider applications [9], [10].

Stator wound field synchronous machines (SWFSMs), including dc-excited multitoothed switched reluctance machines [11], [12], stator dc-excited Vernier reluctance machines (DC-VRMs) [13], [14], and variable flux reluctance machines (VFRMs) [15], [16], have a set of DC field excitation windings placed on the stator together with AC armature windings. Therefore, brushes and slip rings are avoided. The rotor robustness and reliability have potential to be better and their maintenance cost has potential to be lower. Moreover, compared with RWFSMs, better thermal management can be achieved in SWFSMs since all excitation sources are mounted on the stator. However, in SWFSMs field windings and armature windings are in the same stator slots, which lead to complex production process and more copper loss.

Therefore, the dc-biased VRM (dc-biased-VRM) with integrated dc field windings and ac armature windings [17], [18] is proposed to solve the problem. The integrated field and armature windings are connected in parallel to form a single stator winding, thus, the resistance is reduced by half, which helps reduce the copper loss and improve the efficiency [19]. The armature winding current waveforms are sinusoidal with dc bias [20], [21]. The dc-biased current can flexibly change the virtual rotor flux, which assures a superior flux regulation capability. The average torque is produced by the interactions of the rotor flux and the stator flux [17]. Meanwhile, the dc-biased-VRM

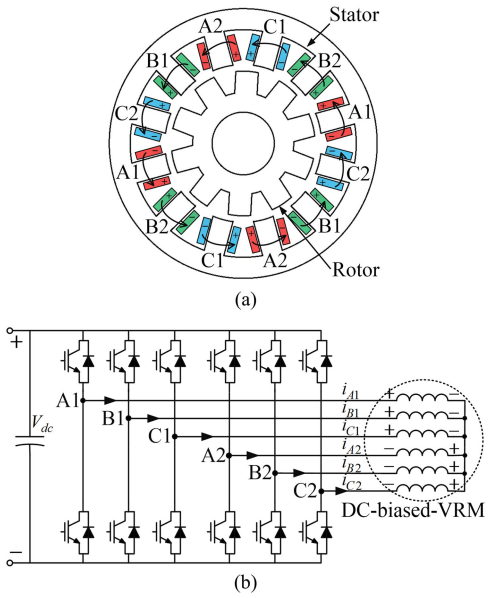

Fig. 1. Structure and corresponding main drive circuit of the 12/10 six-phase dc-biased-VRM. (a) Machine structure. (b) Main drive circuit.

has concentrated stator windings and doubly salient structure, and it makes the machine to have high reliability, low cost, and the heat can be dissipated easily [22]. The dc-biased-VRMs can not only broaden the constant power operation range, but also improve the torque density. With those characteristics, the dc-biased-VRMs can be ideally used for applications which require high speed, variable speed, and operating in severe conditions [23].

For the purpose of realizing the injection of dc-biased current, an integrated field and armature current control strategy is proposed in [20] and [21]. The opposite zero-sequence voltage between the two winding groups generate the zero-sequence current, and the zero sequence current is utilized as the dc-biased current. The *dq*-axis currents are utilized as the ac component [24]–[26]. However, the dc-biased current remains unchanged in the flux weakening region. It restricts the flux regulation ability of dc-biased-VRMs, and the output ability in the flux weakening region is further limited.

In this paper, an optimal three-dimensional current computation flux weakening control strategy for dc-biased-VRMs is illustrated, aiming to maximize the output torque. According to the mathematical model in *dq*0-axis, the voltage and current constraints are explained. Through constructing the Lagrange function, the optimal three-dimensional current distribution is calculated at the intersection of current and voltage constraints. Meanwhile, the optimal current distribution is dependent on the value of inductance. The inductance nonlinearity is reflected by constructing the inductance table to enhance the machine's performance. Finally, the improvements with the proposed flux weakening control strategy are verified experimentally under various operating conditions.

II. Mathematical Model of DC-Biased-VRMs

A. Machine Structure

The structure of the 12/10 six-phase dc-biased-VRM is shown in Fig. 1(a). The coils of one phase are divided into two groups for the purpose of realizing the dc current flow path [17], for example, A1, B1, C1 and A2, B2, C2. The arrows in Fig. 1(a) and (b) represent the reference direction of the ac current. The sign "+" of the armature windings represents the dc-biased current in, and the sign "–" represents the dc-biased current out. The corresponding main drive circuit is shown in Fig. 1(b). The six-phase inverter is associated with the machine in order to provide the dc flow path. With this topology, the dc-biased current can be regulated by adding the opposite zero sequence voltage in the two winding groups.

The phase currents of the two winding groups are as follows:

$$\begin{cases} i_{A1} = I_{\rm ac}\cos(\theta_e) + I_{\rm dc} \\ i_{B1} = I_{\rm ac}\cos(\theta_e - \gamma) + I_{\rm dc} \\ i_{C1} = I_{\rm ac}\cos(\theta_e + \gamma) + I_{\rm dc} \\ i_{A2} = I_{\rm ac}\cos(\theta_e) - I_{\rm dc} \\ i_{B2} = I_{\rm ac}\cos(\theta_e - \gamma) - I_{\rm dc} \\ i_{C2} = I_{\rm ac}\cos(\theta_e + \gamma) - I_{\rm dc} \end{cases} \tag{1}$$

where $I_{\rm ac}$ is the magnitude of the ac armature current component; θ_e is the electrical angle and can be expressed as $\theta_e = N_r\omega_r t$, N_r is the number of rotor slots, ω_r is the rotor mechanical angular speed; and $I_{\rm dc}$ is the dc-biased current in phase windings. For the purpose of simplifying the expression, the electrical angle between different phases is presented as γ in this paper, and γ equals to $2\pi/3$.

The ac component of the two winding groups is exactly the same, and the dc components have the opposite direction. The stator flux produced by ac component in the armature windings. Meanwhile, the rotor flux is flexibly changed by the dc-biased current. The average torque is produced by the interactions of the rotor flux and the stator flux.

B. Mathematical Equations in Synchronous Rotating Frame

The self-inductance and mutual inductance waveforms and fast Fourier transform distributions are shown in Fig. 2. The waveforms are obtained from the 12/10 six-phase dc-biased-VRM finite element analysis (FEA) model, and the phase current is the rated 19 A. L_{A1A1} is the self-inductance of phase A1. M_{A1B1} is the mutual inductance between phases A1 and B1 (two different phases of the same winding group). M_{A1A2} is the mutual inductance between phases A1 and A2 (the same phases of two different winding groups). M_{A1B2} is the mutual inductance between phases A1 and B2 (two different phases of two different winding groups).

As shown in the harmonic analysis in Fig. 2(b), the amplitude of first-order harmonic is comparable with the constant component. The average torque is produced by the interaction of constant component and the fundamental component of inductance [17]–[19]. Hence, the constant component and the fundamental component are analyzed in the mathematical model to simplify the expression.

The steady-state voltage equation for the six-phase dc-biased-VRM in the synchronous rotating frame [20] is given by

$$\boldsymbol{u}_{dq0} = R_s\boldsymbol{i}_{dq0} + \omega_e {L_{dq0}}'i_{dq0} \tag{2}$$

where $\boldsymbol{u}_{dq0} = [u_{d1},\ u_{q1},\ u_{01},\ u_{d2},\ u_{q2},\ u_{02}]^T$ is the *dq*0-axis voltage vector. u_{d1}, u_{q1}, and u_{01} are *dq*0-axis voltages for winding ABC1, and u_{d2}, u_{q2}, and u_{02} are *dq*0-axis voltages for winding ABC2. The *dq*0-axis current vector has the similar ex-

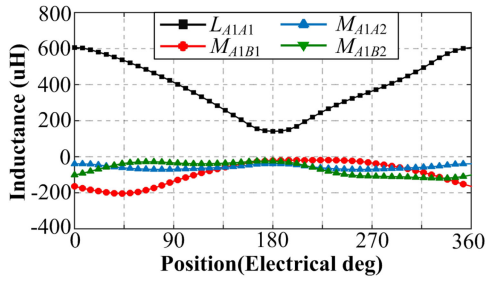

(a)

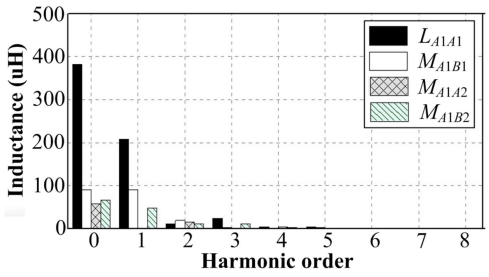

(b)

Fig. 2. Inductance waveforms and harmonics of the 12/10 dc-biased-VRM FEA model. (a) Inductance waveforms. (b) Harmonics.

pression $\boldsymbol{i}_{dq0} = [i_{d1},\, i_{q1},\, i_{01},\, i_{d2},\, i_{q2},\, i_{02}]^T$. $\boldsymbol{L}'_{dq0}$ is the coupling inductance, when the alternating inductance components are neglected, it is expressed as

$$L_{dq0}{}' = \left[\begin{array}{c:c} L_{dq0}{}'_{(3\times3)} & M_{dq0}{}'_{(3\times3)} \\ \hdashline M_{dq0}{}'_{(3\times3)} & L_{dq0}{}'_{(3\times3)} \end{array}\right] \tag{3-a}$$

$$L_{dq0}{}'_{(3\times3)} = \begin{bmatrix} 0 & -(L_1+M_1) & 0 \\ L_1+M_1 & 0 & L_\delta - M_{1\delta} \\ 0 & 0 & 0 \end{bmatrix} \tag{3-b}$$

$$M_{dq0}{}'_{(3\times3)} = \begin{bmatrix} 0 & -(M_2-M_3) & 0 \\ M_2-M_3 & 0 & M_{2\delta}+M_{3\delta} \\ 0 & 0 & 0 \end{bmatrix} \tag{3-c}$$

where L_1 is the self-inductance of the stator winding. M_1 is the mutual inductance for two different phases of the same winding group. M_2 is the mutual inductance for the same phases of two different winding groups. M_3 is the mutual inductance for different phases of two different winding groups. L_δ is the fundamental component of self-inductance. $M_{1\delta}$ is the fundamental component of mutual inductance for two different phases of the same winding group. $M_{2\delta}$ is the fundamental component of mutual inductance for the same phases of two different winding groups. $M_{3\delta}$ is the fundamental component of mutual inductance for different phases of two different winding groups.

In the six-phase dc-biased-VRM, the ac component of the two winding groups is exactly the same, and the dc component has the opposite direction. It can be presented in *dq*0-axis currents as follows: $i_{d1} = i_{d2} = i_d$, $i_{q1} = i_{q2} = i_q$, $i_{01} = -i_{02} = i_0$. Define $L_s = L_1 + M_1 + M_2 - M_3$, and $L_0 = L_\delta - M_{1\delta} + M_{2\delta} + M_{3\delta}$, and the *dq*0-axis voltage components in (2) can be expressed as

$$\begin{cases} u_{d1} = R_s i_d - \omega_e L_s i_q \\ u_{q1} = R_s i_q + \omega_e L_s i_d + \omega_e L_0\, i_0 \\ u_{01} = R_s i_0 \end{cases} \tag{4-a}$$

$$\begin{cases} u_{d2} = R_s i_d - \omega_e L_s i_q \\ u_{q2} = R_s i_d + \omega_e L_s i_d + \omega_e L_0\, i_0 \\ u_{02} = -R_s i_0. \end{cases} \tag{4-b}$$

From (4), the *dq*-axis inductance has the equal value. The electromagnetic torque is generated by the sum of two winding groups, and it can be obtained by calculating the cross product of the total linkage flux and current vectors in the *dq*0-axis, where n_r is the number of rotor slots

$$T_e = 3 n_r L_0 i_q i_0. \tag{5}$$

C. Voltage and Current Constraints

The operating point (i_d, i_q, i_0) is constrained by the voltage and current limitations. The maximum current rms value $i_{\max}$ is determined by the machine thermal rating [12]. The constant amplitude transformation matrix is used in this paper, and the current limit circle is expressed as [27], [28]

$$i_{s1}{}^2 = \left(\frac{i_d}{\sqrt{2}}\right)^2 + \left(\frac{i_q}{\sqrt{2}}\right)^2 + i_0{}^2 \le i_{\max}{}^2 \tag{6}$$

where i_{s1} is the armature current rms value of winding ABC1. The current limit circle for winding ABC2 is exactly the same.

The maximum voltage $u_{\max}$ that the inverter can supply to the machine is limited by the dc-link voltage and the pulsewidth modulation (PWM) strategy [29]. This paper is based on space vector PWM, and $u_{\max}$ is $V_{\rm dc}/\sqrt{3}$ [20]. The voltage limit equation for winding ABC1 is

$$u_{s1} = \sqrt{u_{d1}{}^2 + u_{q1}{}^2 + u_{01}{}^2} \le u_{\max} \tag{7}$$

where u_{s1} is the armature terminal voltage of winding ABC1.

The phase resistance of the dc-biased-VRM is relatively small. When the machine is operating stably, the inductance voltage drop takes the leading role, and the resistance voltage drop is neglected. Substituting (4-a) into (7) and neglecting the resistance voltage drop, (7) can be rewritten in the form of (8). The voltage constraint is expressed as a circle in the *dq*-axis whose center is $(-L_0 i_0 \,/\, L_s, 0)$, and the radius is $u_{\max} \,/\, (L_s \omega_e)$

$$\frac{\left(i_d + \frac{L_0}{L_s} i_0\right)^2}{\left(u_{\max}/\left(L_s\omega_e\right)\right)^2} + \frac{i_q{}^2}{\left(u_{\max}/\left(L_s\omega_e\right)\right)^2} \le 1. \tag{8}$$

The voltage constraint can also be expressed as an ellipse in the *q*0-axis, whose center is $(-L_s\, i_d \,/\, L_0, 0)$, the radius is $u_{\max} \,/\, (L_s\omega_e)$, and $u_{\max} \,/\, (L_0\omega_e)$. The voltage limit equation for winding ABC2 is exactly the same

$$\frac{\left(i_0 + \frac{L_s}{L_0} i_d\right)^2}{\left(u_{\max}/\left(L_0\omega_e\right)\right)^2} + \frac{i_q{}^2}{\left(u_{\max}/\left(L_s\omega_e\right)\right)^2} \le 1. \tag{9}$$

III. Conventional Flux Weakening Control Strategy

In order to maximize the output torque in the whole operating range, the optimal set of i_d, i_q, and i_0 needs to be found.

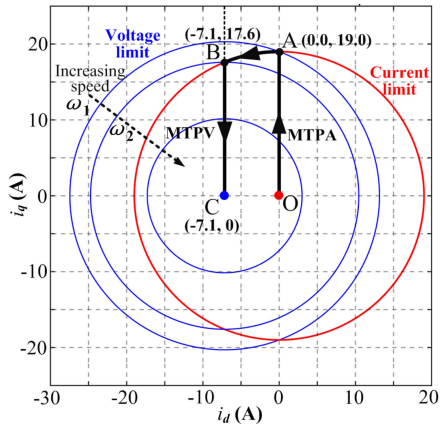

Fig. 3. Current trajectory of the conventional control strategy in *dq*-plane.

In the conventional flux weakening control strategy, the 0-axis current i_0 is fixed at $0.707 i_{\max}$ [21]. The airgap flux is weakened by applying the negative *d*-axis current, which is similar to the control strategy for surface-mounted PMSMs. The current trajectory gives the maximum output torque when $i_0 = 0.707 i_{\max}$ at three operating regions.

A. Constant Torque Operating Region ($\omega \le \omega_1$)

In the constant torque operating region, the maximum torque per ampere control strategy with optimal dc and ac components is adopted [12], and $i_0 = 0.707 i_q$, $i_d = 0$. From (5) and (6), the maximum output torque can be achieved on the edge of the current limit circle. At the moment, $i_d = 0$, $i_q = i_{\max}$, and $i_0 = 0.707 i_{\max}$. Fig. 3 shows the optimal current trajectory of the conventional control strategy in the *dq*-plane. The base speed ω_1 is the onset speed of flux weakening operation. It can be expressed at the intersection of current limit circle and the voltage limit circle of ω_1, shows in point A. For the dc-biased-VRM having $i_{\max} = 19$ A, $u_{\max} = 20$ V, and $\omega_1 = 500\ \pi$rad/ s, the point A has the coordinates in the *dq*-plane of (0.0, 19.0), and the corresponding i_0 is fixed at the value of 13.4 A.

B. Flux Weakening Operating Region I ($\omega_1 < \omega \le \omega_2$)

For speed over ω_1, the optimal current trajectory is at the intersection of the current limit circle and voltage limit circle. At the moment, $i_{s1} = i_{\max}$ and $u_{s1} = u_{\max}$. For the dc-biased-VRM having $L_s = 596.3\ \mu$H and $L_0 = 317.1\ \mu$H, the coordinates of point B can be calculated from (6) and (8) of speed ω_2. As shown in Fig. 3, with the increment of the rotational speed, the current trajectory moves along the current limit circle from point A (0.0, 19.0) to point B (–7.1, 17.6).

C. Flux Weakening Operating Region II ($\omega > \omega_2$)

The speed ω_2 is the onset speed of the flux weakening region II. It can be expressed in the optimal current trajectory at point B. For the speed over ω_2, the optimal current trajectory is on the maximum torque per voltage (MTPV) line. At the moment, $i_{s1} < i_{\max}$ and $u_{s1} = u_{\max}$. The optimal current trajectory moves from B to C as the rotational speed increases. Point C corresponds to the theoretical maximum speed, and it has the coordinates of (–7.1, 0). The current trajectory is only constrained by the voltage limit circle, and the current constraint is not fully utilized. It restricts the output capacity of the dc-biased-VRM.

IV. Proposed Flux Weakening Control Strategy

The conventional i_0-fixed flux weakening control strategy is simple to be implemented, however, the 0-axis current is not utilized as an additional degree of freedom. To achieve the maximum torque capability in the flux weakening region, the proposed three-dimensional current computation flux weakening control strategy is introduced. The current trajectory is transformed from the *dq*-plane into the three-dimensional *dq*0-plane.

A. Solution of the Optimal Three-Dimensional Currents

When i_0 is utilized as an additional degree of freedom, the optimal current trajectory is transformed into the three-dimensional *dq*0-plane. The optimal operating point (i_d, i_q, i_0) can be calculated by adopting the Lagrange method. To simplify the calculation process, the target function is replaced by

$$T = \ln(i_q i_0) = \ln i_q + \ln i_0. \tag{10}$$

By using (6) and (8) as the constraint equations, and (10) as the target function, the Lagrange function is expressed in (11), where λ_1 and λ_2 are Lagrange multipliers

$$F(i_d, i_q, i_0, \lambda_1, \lambda_2) = \ln i_q + \ln i_0 + \lambda_1 \left((-L_s i_q)^2 + (L_s i_d + L_0 i_0)^2 - (u_{s1}/\omega_e)^2 \right) + \lambda_2 \left(\frac{{i_d}^2}{2} + \frac{{i_q}^2}{2} + {i_0}^2 - {i_{s1}}^2 \right). \tag{11}$$

Then, the necessary conditions for the optimal solutions are expressed as

$$\begin{cases} \partial F(i_d, i_q, i_0, \lambda_1, \lambda_2)/\partial i_d = 2\lambda_1 \left({L_s}^2 i_d + L_s L_0 i_0 \right) + \lambda_1 i_d = 0 \\ \partial F(i_d, i_q, i_0, \lambda_1, \lambda_2)/\partial i_q = \frac{1}{i_q} + 2\lambda_1 {L_s}^2 i_q + \lambda_2 i_q = 0 \\ \partial F(i_d, i_q, i_0, \lambda_1, \lambda_2)/\partial i_0 = \frac{1}{i_0} + 2\lambda_1 \left({L_0}^2 i_0 + L_s L_0 i_d \right) + 2\lambda_2 i_0 = 0 \\ \partial F(i_d, i_q, i_0, \lambda_1, \lambda_2)/\partial \lambda_1 = \frac{{i_d}^2}{2} + \frac{{i_q}^2}{2} {i_0}^2 - {i_{s1}}^2 = 0 \\ \partial F(i_d, i_q, i_0, \lambda_1, \lambda_2)/\partial \lambda_2 = (L_s i_q)^2 + (L_s i_d + L_0 i_0)^2 - (u_{s1}/\omega_e)^2 = 0. \end{cases} \tag{12}$$

The analytical solution is finally obtained by solving (12), and it is expressed as

$$\begin{cases} i_0 = \sqrt{\dfrac{2{L_s}^2 \left({L_0}^2 + 2{L_s}^2 \right) {i_{s1}}^2 + \left({L_0}^2 - 2{L_s}^2 \right) \frac{{u_{s1}}^2}{{\omega_e}^2}}{{L_0}^2 + 2{L_s}^2}} \\ i_d = \dfrac{L_s L_0}{{L_0}^2 - 2{L_s}^2} \left(4 i_0 - \dfrac{2{i_{s1}}^2}{i_0} \right) \\ iq = \sqrt{2{i_{s1}}^2 - {i_d}^2} - 2{i_0}^2. \end{cases} \tag{13}$$

If the current vector is controlled according to (13), the resultant armature terminal voltage u_{s1} is always kept within $u_{\lim}$. Fig. 4 shows all the aforementioned boundaries and current trajectory. Fig. 4(a) is the operating range in the *dq*-plane. The black bold line is the optimal current trajectory for the dc-biased-VRM. For any given torque, dc bus voltage, and motor speed, there exists torque curve and voltage-limit ellipse. The current vector producing maximum torque at a given speed is given by

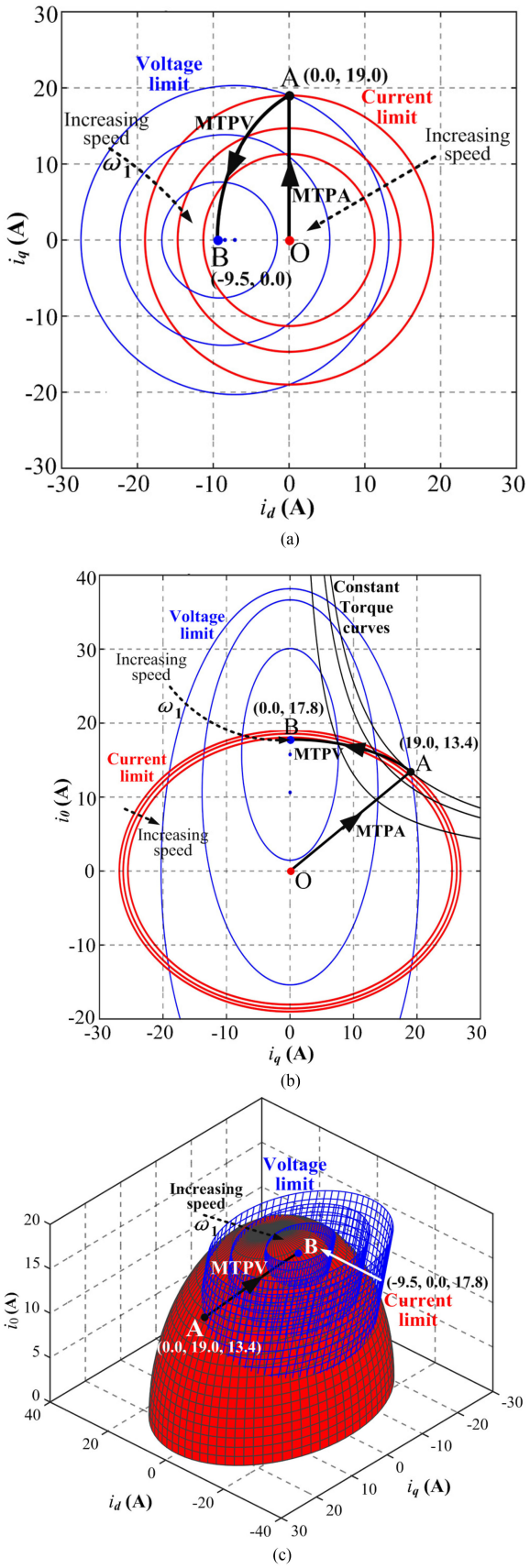

Fig. 4. Constraints and optimal current trajectory of the proposed control strategy. (a) Operating range in dq-plane. (b) Operating range in $q0$-plane. (c) Operating range in three-dimensional $dq0$-plane.

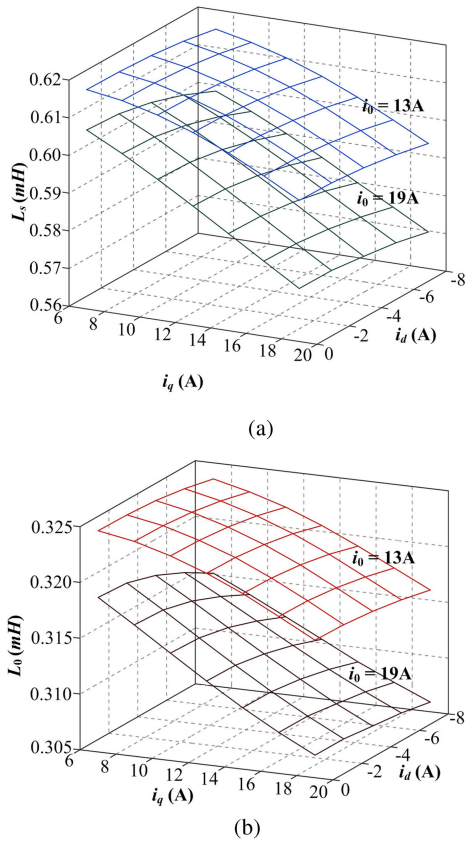

Fig. 5. Inductance variation depending on currents (FEM results). (a) L_s with $i_0 = 13$ A and 19 A. (b) L_0 with $i_0 = 13$ A and 19 A.

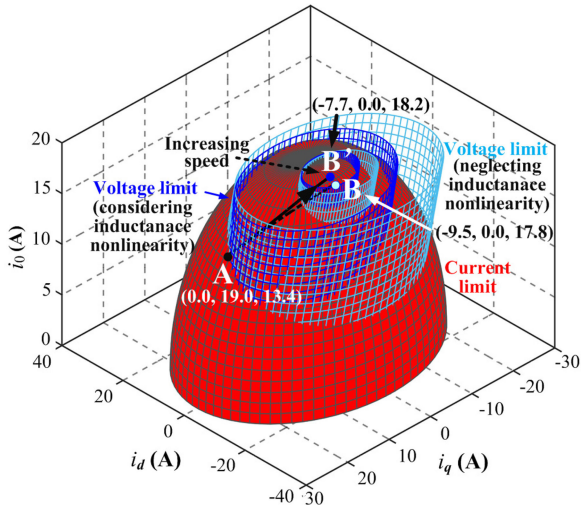

Fig. 6. Constraints and optimal current trajectory of the proposed control strategy in three-dimensional $dq0$-plane considering inductance nonlinearity.

the cross point of the current-limit circle and the voltage-limit ellipse. Different from the conventional i_0-fixed control strategy. The current-limit circle shrinks with the increment of rotational speed, and it is due to the increment of i_0. The proposed control strategy utilizes both the voltage and current constraints in the whole flux weakening region. The adjustable dc-biased current assures a superior flux regulation capability, and the output capacity is expected to be maximized.

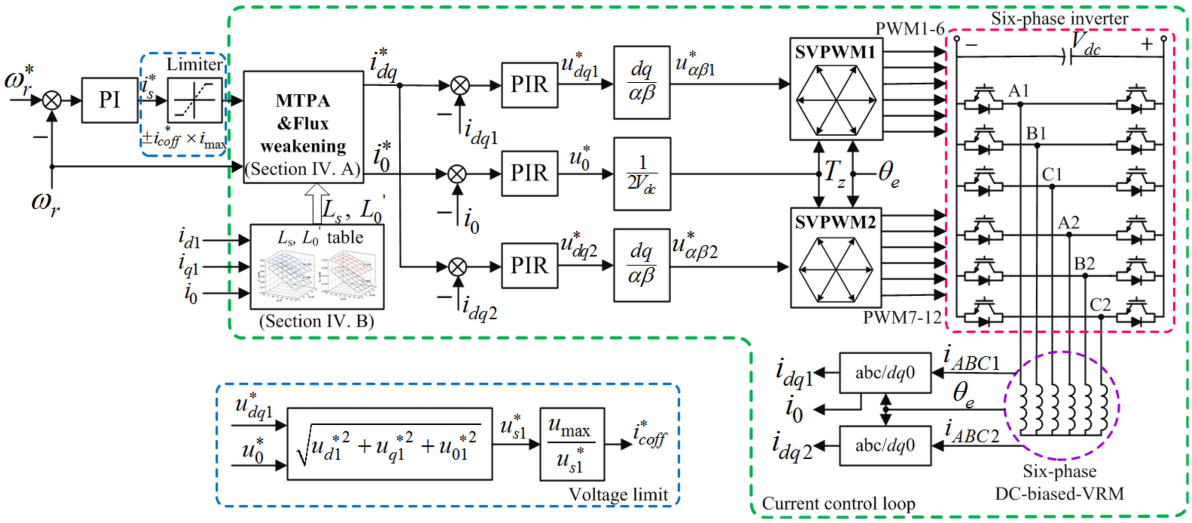

Fig. 7. Overall block diagram of the proposed flux weakening control strategy for six-phase dc-biased-VRMs.

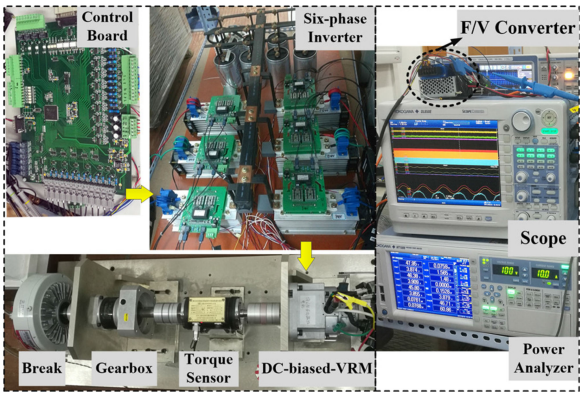

Fig. 8. Picture of the experimental setup.

Fig. 4(b) shows the operating range in the $q0$-plane. The voltage constraint is the blue ellipse, and with the increment of rotational speed, the center of the voltage ellipse moves upward along with i_0-axis. The current-limit circle shrinks with the increment of rotational speed, and it is due to the increment of i_d. Fig. 4(c) shows the operating range in three-dimensional $dq0$-plane. When operating in the flux weakening region, the optimal current trajectory, which provides the maximum output torque, is at the intersection of the current limit surface and voltage limit surface. At the moment, $i_{s1} = i_{\max}$ and $u_{s1} = u_{\max}$. Point B corresponds to the theoretical maximum speed. With the increment of the rotational speed, the current trajectory is the black bold line from point A (0.0, 19.0, 13.4) to point B (–9.5, 0.0, 17.8).

B. Inductance Nonlinearity Effect on Three-Dimensional Current Computation

One difficult problem in the operation of dc-biased-VRM is that the different combinations of (i_d, i_q, i_0) contribute to the variation in the inductance. The variation in the inductance leads to the deviation of the optimal current trajectory, and it should be considered in order to enhance the machine's performance.

Fig. 5(a) shows the finite-element method (FEM) results of L_s versus $-20\,\text{A} \leqslant i_d \leqslant 0$ and $0 \leqslant i_q \leqslant 20\,\text{A}$ for different 0-axis currents, $i_0 = 13$ and 19 A, respectively. Fig. 5(b) shows L_0 versus $-20\,\text{A} \leqslant i_d \leqslant 0$ and $0 \leqslant i_q \leqslant 20\,\text{A}$ for different 0-axis currents, $i_0 = 13$ and 19 A, respectively. The two figures indicates that the different combinations of (i_d, i_q, i_0) contribute to the variation in the inductance. By constructing the inductance table, the inductance nonlinearity is reflected in determining the optimal three-dimensional currents of the flux weakening control strategy.

Fig. 6 shows the optimal current trajectory considering the inductance nonlinearity in three-dimensional $dq0$-plane. The voltage-limit surface begins to shrink when the inductance nonlinearity is considered, compared with the current trajectory neglecting inductance nonlinearity (the black bold line from point A to point B). With the increment of the rotational speed, the optimal current trajectory moves upward along with the current-limit surface. The optimal current trajectory considering inductance nonlinearity is the black bold line from point A (0.0, 19.0, 13.4) to point B' (−7.7, 0.0, 18.2).

The overall control algorithm of the six-phase dc-biased-VRM is shown in Fig. 7. Due to the asymmetries in the stator winding sets and applied voltages, ABC1 and ABC2 winding groups have independent current regulators [20]. The 0-axis reference current $i_{01} = -i_{02} = i_0$, and the 0-axis feedback current i_0 is obtained from i_{ABC1} through rotating coordinate transformation. The dc-biased current is regulated by adding the opposite zero sequence voltage in the two winding groups, and the zero sequence voltage is determined by the closed-loop current controller in the 0-axis. The $dq0$-axis current references are generated by the three-dimensional current computation in Section IV-A, and the inductance values are reflected by the inductance table in Section IV-B. The armature terminal voltage is limited by the blue box in Fig. 7. When the voltage reference u_{s1}^* exceeds the maximum voltage $u_{\max}$, the current reference i_s^* decreases until the output voltage is smaller than the maximum value. The back electromotive force (EMF) waveforms of the machine contain plenty of harmonics [28]. Due to the limited ac signal tracking capability, the PI current regulator in the synchronous rotating coordinate cannot eliminate the current distortion caused by the distorted EMF

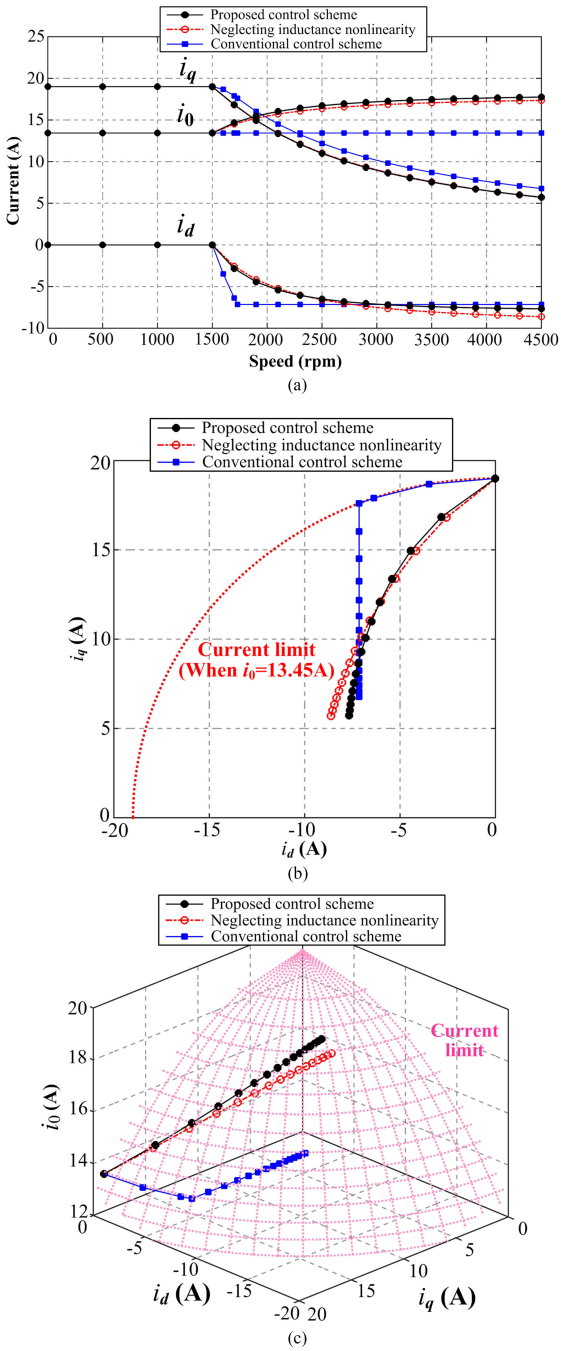

Fig. 9. Comparisons of current trajectories between conventional and proposed flux weakening control strategy. (a) i_d, i_q, and i_0 versus speed. (b) Current trajectory in dq-plane. (c) Current trajectory in $dq0$-plane.

[30]. The $dq0$-axis currents are regulated by proportional integral and resonant (PIR) regulators [31].

V. Experimental Results

The effectiveness of the proposed optimal three-dimensional current computation flux weakening control strategy was validated experimentally through a prototype 12/10 six-phase dc-biased-VRM. The parameters of the machine are listed in Table II. The picture of the experimental setup is shown in Fig. 8. The control board is based on TMS320F28335, and the dc-biased-VRM is driven by a six-phase inverter. The sampling frequency and IGBT switching frequency are both 20 kHz. The input power is calculated by a Yokogawa WT1800 precision power analyzer. The output torque and output power are tested by JN338 torque-speed sensor. The output signal for the torque-speed sensor is transformed by F/V converter. All the experimental waveforms are captured from Yokogawa DL850E multiple-channel oscilloscope.

A. Steady-State Characteristics

Fig. 9 shows the steady-state comparisons between the proposed and conventional flux weakening method. The load is changed gradually to assure the maximum output torque. In this way, the terminal voltage reaches the maximum voltage $u_{\max}$ at 1500 r/min, and the motor operates in the flux weakening region above 1500 r/min. Fig. 9(a) shows the current–speed characteristics. In the conventional control method, see the blue curve in Fig. 9(a), the 0-axis current is always kept at 13.45 A, and i_d and i_q are controlled according to the analysis in Section III. In the proposed control method, the 0-axis current is utilized as an additional degree of freedom. This provides the potential of generating higher torque for the dc-biased-VRM. The optimal current trajectory considering inductance nonlinearity is the black bold line in Fig. 9(a), and the current trajectory neglecting inductance nonlinearity is the red dotted line. Figs. 9(b) and (c) show the improvement of the current trajectory in the dq-plane and three-dimensional $dq0$-plane, respectively. In the conventional method, when the machine is operating over 2300 r/min, the current trajectory is only constrained by the voltage limit circle shown in Fig. 9(b). It restricts the output capacity of dc-biased-VRMs, compared with the current trajectory neglecting inductance nonlinearity (the red dotted line). With the increment of the rotational speed, the optimal current trajectory moves upward along with the current-limit surface, see the black bold line.

Characteristic curves of the conventional and proposed flux weakening control strategy are shown in Fig. 10. Figs. 10(a) and (b) show the output torque and power is enlarged with the proposed flux weakening control strategy. The output power in the flux weakening range with the conventional flux weakening control strategy should be constant if the inductance nonlinearity is neglected. However, the inductance varies with the current distribution. The torque command decreases in order to maintain the armature voltage within $u_{\max}$. As a result, the output power starts to descend in the flux weakening range.

Figs. 10(c) and (d) show the armature terminal voltage-speed curve and the armature current-speed curve, respectively. All the three control methods restrict the armature terminal voltage within the maximum voltage. However, as shown in Fig. 10(d), in order to maintain the armature voltage within the voltage constraint, the armature current decreases slightly when operating with the control strategy neglecting inductance nonlinearity. Meanwhile, the armature current decreases apparently with the conventional method above 1700 r/min. The armature current is not fully utilized with the two methods, only the proposed method utilizes the armature current at the maximum value. The proposed method utilizes both the voltage and current constraint in the whole operating range, and as a result, the output capacity is enhanced.

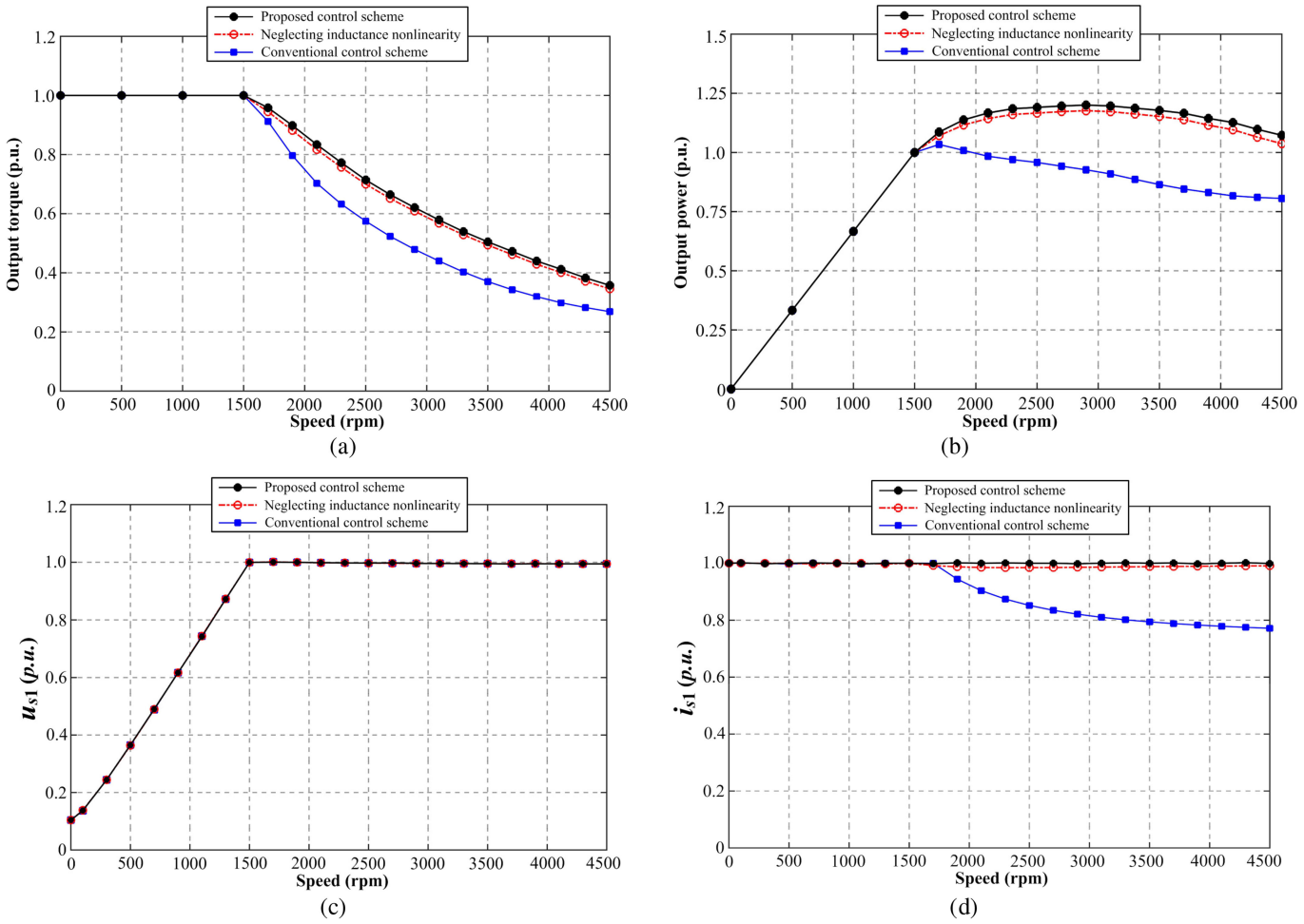

Fig. 10. Characteristic curves of conventional and proposed flux weakening control strategy. (a) Torque-speed curve. (b) Output power-speed curve. (c) Voltage-speed curve. (d) Current-speed curve.

Fig. 11 shows the efficiency-speed curve of the dc-biased-VRM with the conventional and proposed flux weakening control strategy, including the efficiency of the machine side in Fig. 11(a), and the overall control system in Fig. 11(b). The operating efficiency is calculated by the power analyzer and torque meter every 200 r/min. The efficiency on the machine is increased by 6.2% with the proposed method at 2900 r/min in Fig. 11(a). The value for the control system is increased by 5.3% with the proposed method at 2900 r/min in Fig. 11(b). The efficiency increased with the proposed method in the flux weakening region. Although the phase current increased with the proposed method, the energy losses caused by the increased current are smaller than the increment of the output power.

Fig. 12 shows the experimental waveforms of the proposed flux weakening control strategy at different speeds. Fig. 12(a) shows the waveforms at 1500 r/min. The d-axis current is 0 A, the q-axis current is 19 A, and the 0-axis current is 13.45 A. The ac component of phases A1 and A2 is exactly the same, and the dc component has the opposite direction. Fig. 12(b) shows the waveforms at 2500 r/min. The d-axis current is –6.5 A, the q-axis current is 11.0 A, and the 0-axis current is 16.7 A. The armature voltage u_{s1} stays unchanged at the value of 20 V, which is within the voltage limit. Fig. 12(c) shows the waveforms at 3500 r/min. The d-axis current is –7.4 A, the q-axis current is 7.5 A, and the 0-axis current is 17.5 A. Fig. 12(d) shows the waveforms at 4500 r/min. The d-axis current is –7.7 A, the q-axis current is 5.7 A, and the 0-axis current is 17.8 A. The armature voltage also remains unchanged.

B. Dynamic Characteristics

Fig. 13 shows the experimental results of the conventional and the proposed method under the same load. The motor operates with the conventional method at first, and the load torque reaches the maximum value of the conventional method. The transition of the proposed method occurs at the dotted line. Fig. 13(a) and (b) shows the waveforms at 2500 and 3500 r/min, respectively. After the transition of the proposed method, the armature terminal voltage decreased, and it is within the voltage constraint. The output torque has the ability continue to increase, and the proposed method has better output capacity.

In Fig. 14, the experiments of the conventional method and the proposed method were performed with motor speed acceleration from 0 to 4500 r/min. The process includes transition from the constant torque region to the flux weakening region at the speed of 1500 r/min, also known as the base speed. The speed reference is given by a ramp function, and the motor is accelerated with the maximum torque in the flux weakening region. Fig. 14(a) shows the experimental results of the conventional

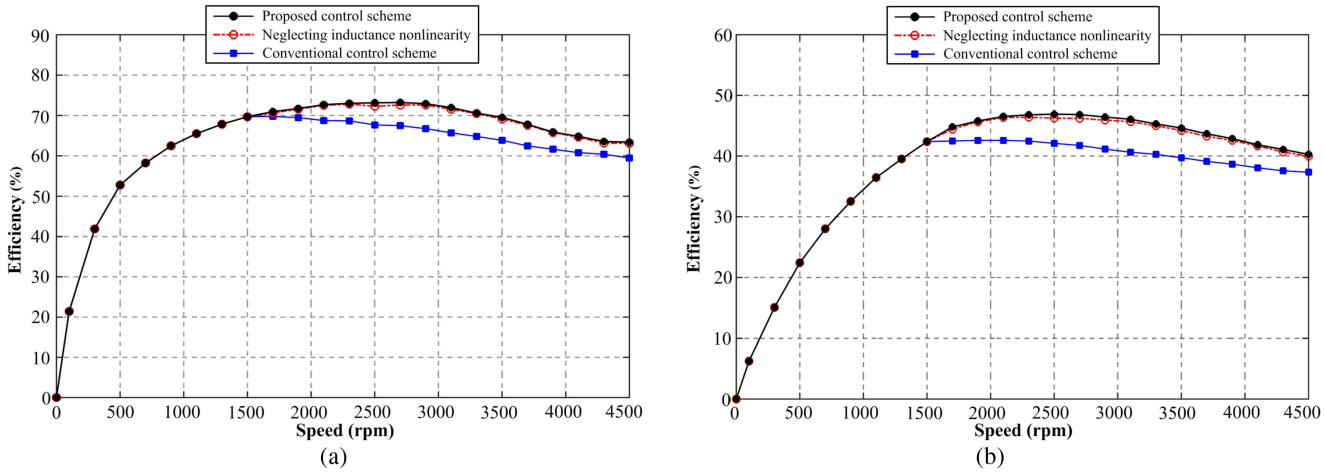

Fig. 11. Efficiency-speed curve of the dc-biased-VRM with the conventional and proposed flux weakening control strategy. (a) Machine side efficiency. (b) Control system efficiency.

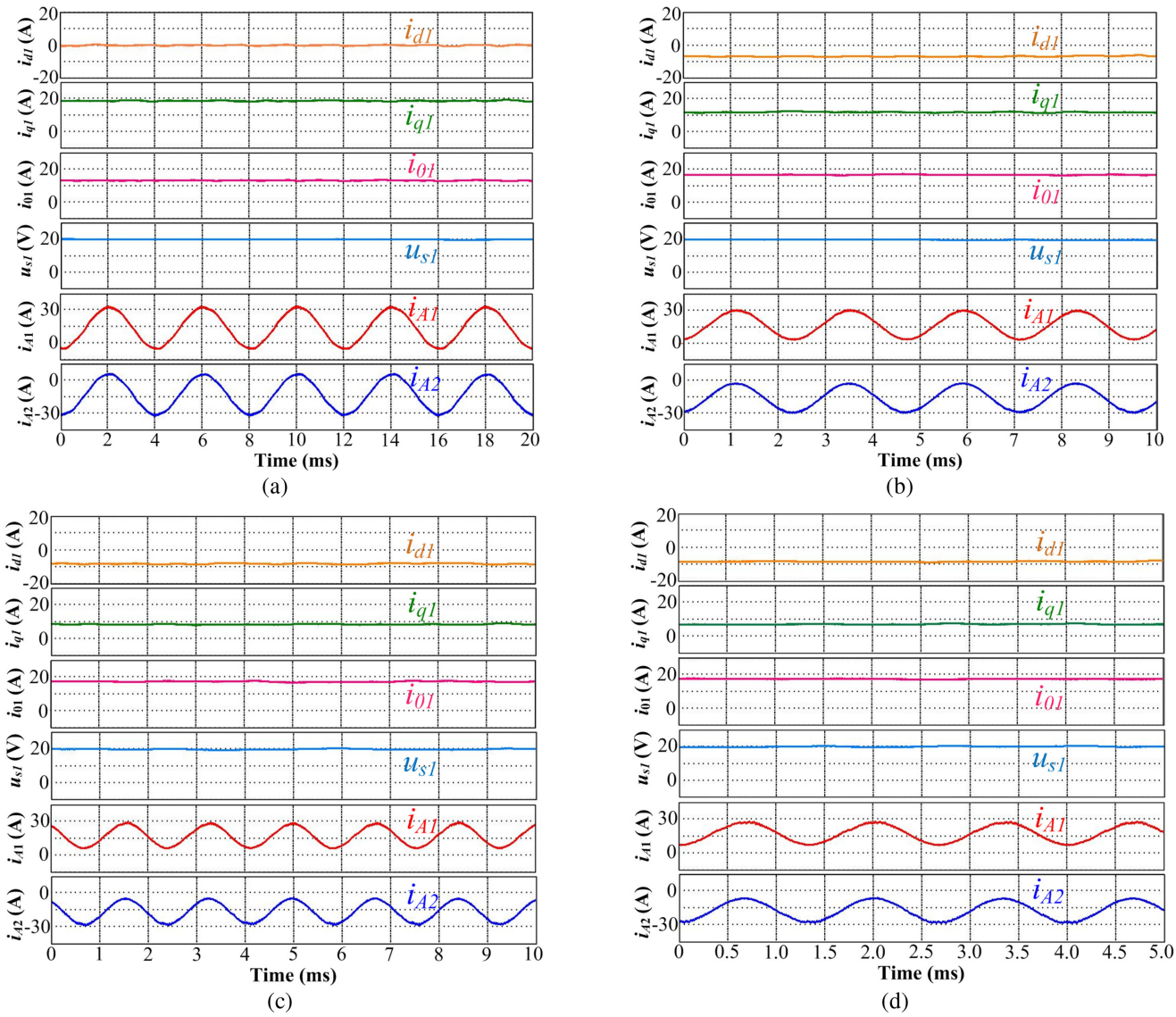

Fig. 12. Experimental waveforms of the proposed flux weakening control strategy. (a) At 1500 r/min. (b). At 2500 r/min. (c). At 3500 r/min. (d). At 4500 r/min.

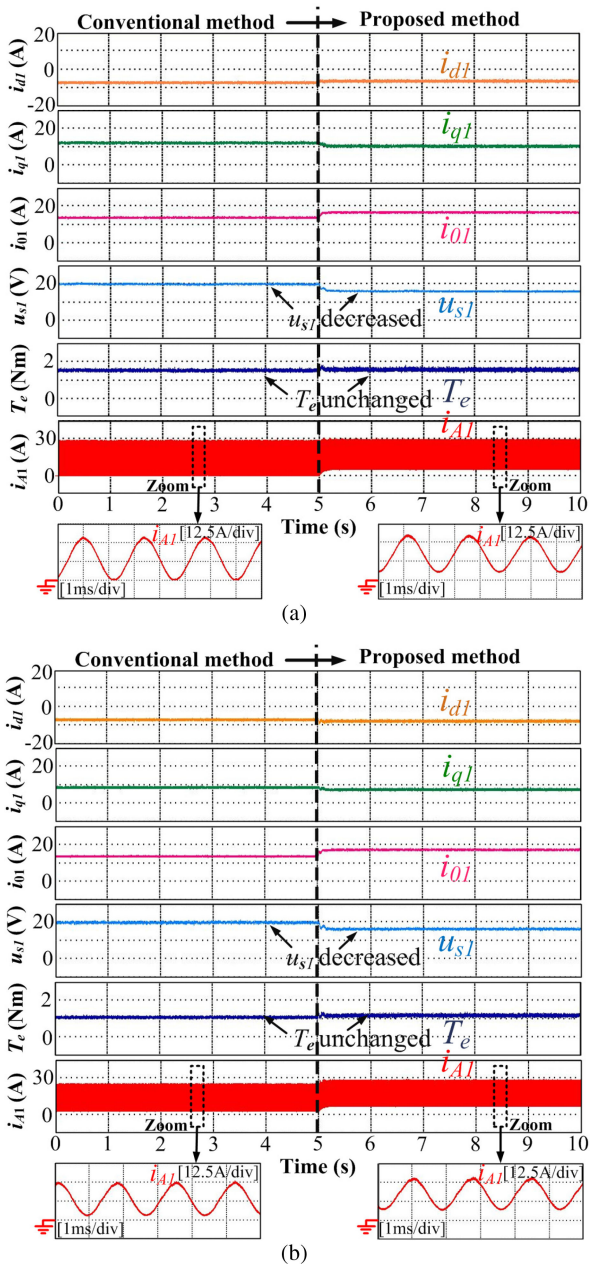

Fig. 13. Experimental results of the conventional and the proposed method under the same load. (a) At 2500 r/min. (b) At 3500 r/min.

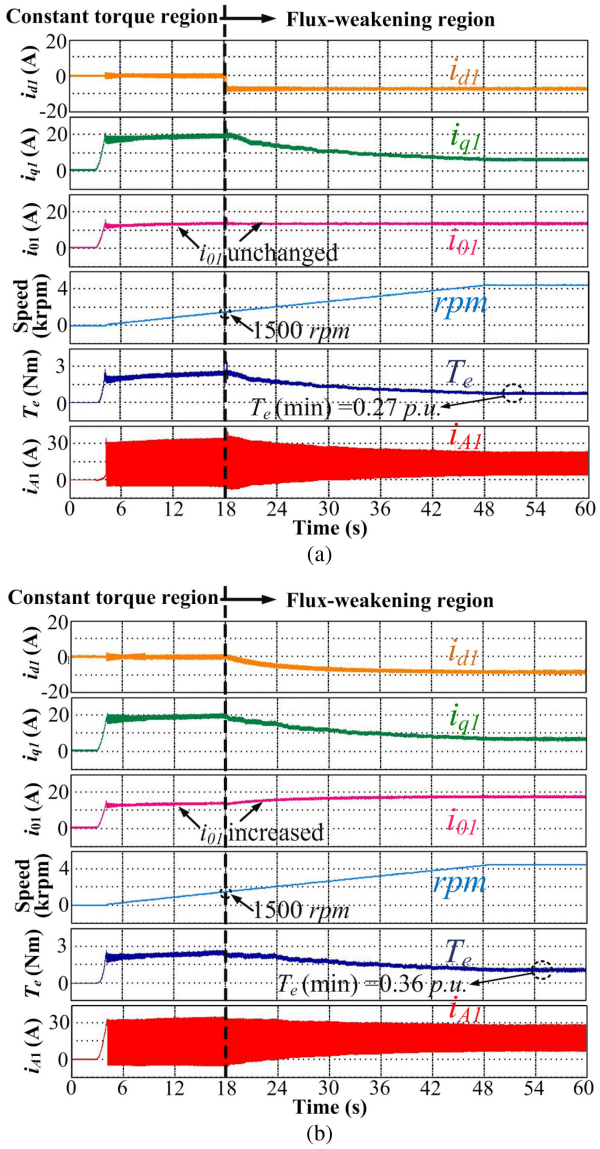

Fig. 14. Comparisons between the conventional and the proposed method from standstill to 4500 r/min. (a) Conventional method. (b). Proposed method.

method. The voltage limit shrinks with the increase in the motor speed. i_0 remains unchanged, and the required i_d is getting smaller. Then, the optimal current trajectory is on the MTPV line. i_d is fixed at –7.1 A and i_q is getting smaller to maintain the voltage constraint. Fig. 14(b) shows the experimental results of the proposed method. The current vector is controlled to follow the cross point of the current-limit circle and the voltage-limit ellipse above the base speed. With the increment of the rotor speed, the required i_0 is getting larger, i_d and i_q are getting smaller gradually until the motor speed reached its maximum value. The output torque was more than 32% continuously by utilizing the proposed algorithm.

The summary of the output torque increment with the proposed flux weakening control strategy is shown in Table I.

TABLE I
SUMMARY OF THE OUTPUT TORQUE INCREMENT IN THE FLUX WEAKENING REGION

Rotational speed (rpm)	Output torque (Nm)		Torque increment (%)
	Conventional method	Proposed method	
1500	2.16	2.16	0.00 %
2000	1.64	1.88	14.63 %
2500	1.26	1.55	23.02 %
3000	1.02	1.30	27.45 %
3500	0.80	1.09	36.25 %
4000	0.74	0.97	31.08 %
4500	0.58	0.77	32.76 %

Taking the output torque at 3500 r/min, for example, the output toque is 0.80 N·m when operating with the conventional method. The value increased to 1.09 N·m with the proposed method. The output torque increased 36.25%. Hence, the approach presented in this paper effectively enhances the output capacity of the dc-biased-VRM in the flux weakening region.

VI. Conclusion

This paper presents a control strategy that maximizes the output torque in the flux weakening region for dc-biased-VRMs. Compared with the conventional method, which uses the fixed 0-axis current, the proposed method utilizes the 0-axis current as the additional degree of freedom, and the current trajectory is transformed from the *dq*-plane into the three-dimensional *dq*0-plane. The voltage limit ellipse changes its profile depending on the 0-axis current, and its intersection with the current limit circle will be a candidate solution in the three-dimensional *dq*0-plane. The optimal three-dimensional current distribution is calculated by a Lagrange function, and it is dependent on L_s and L_0. The inductance nonlinearity is reflected by constructing the inductance table. The algorithm provides maximum torque capability and high efficiency for dc-biased-VRMs despite the changes in inductance parameters in the flux weakening region. The validity of the proposed algorithm is verified by experimental results for steady and dynamic operations. It is proven that the proposed method can achieve the purpose of enhance the output ability, and effectively improve the efficiency at the same time.

Appendix

TABLE II
Parameters of the Prototype DC-Biased-VRM

Parameters	Symbol	Values
Stator slot number	n_s	12
Rotor slot number	n_r	10
Stator outer diameter (mm)		124
Axial length (mm)		105
Phase resistance (Ω)	R_s	0.044
Stator inductance (μH)	L_s	596.3
0-axis inductance (μH)	L_0	317.1
Maximum current (A)	i_{max}	19
Maximum voltage (V)	u_{max}	20
Base speed (rpm)	n_{base}	1500
Output power (W)	P_N	345

References

[1] S. R. Macminn and T. M. Jahns, "Control techniques for improved high-speed performance of interior PM synchronous motor drives," *IEEE Trans. Ind. Appl.*, vol. 27, no. 5, pp. 997–1004, Sep./Oct. 1991.

[2] J. Lee, K. Nam, S. Choi, and S. Kwon, "Loss-minimizing control of PMSM with the use of polynomial approximations," *IEEE Trans. Power Electron.*, vol. 24, no. 4, pp. 1071–1082, Apr. 2009.

[3] D. Li, R. Qu, and T. Lipo, "High-power-factor Vernier permanent magnet machines," *IEEE Trans. Ind. Appl.*, vol. 50, no. 6, pp. 3664–3674, Nov./Dec. 2014.

[4] A. M. El-Refaie, "Fractional-slot concentrated-windings synchronous permanent magnet machines: Opportunities and challenges," *IEEE Trans. Ind. Electron.*, vol. 57, no. 1, pp. 107–121, Jan. 2010.

[5] D. J. Perreault and V. Caliskan, "Automotive power generation and control," *IEEE Trans. Power Electron.*, vol. 19, no. 3, pp. 618–630, May 2004.

[6] Y. Nie, I. P. Brown, and D. C. Ludois, "Deadbeat-direct torque and flux control for wound field synchronous machines," *IEEE Trans. Ind. Electron.*, vol. 65, no. 3, pp. 2069–2079, Mar. 2018.

[7] Y. Kim and K. Nam, "Copper loss-minimizing field current control strategy for wound synchronous machines," *IEEE Trans. Power Electron.*, vol. 32, no. 2, pp. 1335–1345, Feb. 2017.

[8] G. Jawad, Q. Ali, T. A. Lipo, and B. I. Kwon, "Novel brushless wound rotor synchronous machine with zero-sequence third-harmonic field excitation," *IEEE Trans. Magn.*, vol. 52, no. 7, pp. 1–4, Jul. 2016.

[9] X. Liu and Z. Q. Zhu, "Comparative study of novel variable flux reluctance machines with doubly fed doubly salient machine," *IEEE Trans. Magn.*, vol. 49, no. 7, pp. 3838–3841, Jul. 2013.

[10] S. Jia, R. Qu, and J. Li, "Analysis of the power factor of stator DC excited vernier reluctance machines," *IEEE Trans. Magn.*, vol. 51, no. 11, Nov. 2015, Art. no. 8207704.

[11] C. Liu, K. T. Chau, H. T. Li, F. Lin, F. Li, and T. W. Ching, "Magnetic vibration analysis of a new DC-excited multitoothed switched reluctance machine," *IEEE Trans.Magn.*, vol. 50, no. 11, Sep. 2014, Art. no. 8105204.

[12] N. Nakao and K. Akatsu, "Vector control specialized for switched reluctance motor drives," in *Proc. 21st Int. Conf. Electr. Mach.*, Sep. 2014, pp. 937–943.

[13] S. Jia, R. Qu, J. Li, D. Li, and H. Fang, "Principles of stator DC winding excited vernier reluctance machines," *IEEE Trans. Energy Convers.*, vol. 31, no. 3, pp.935–946, Sep. 2016.

[14] S. Jia, R. Qu, J. Li, D. Li, and H. Lu, "Design considerations of stator DC-winding excited vernier reluctance machines based on the magnetic gear effect," *IEEE Trans. Ind. Appl.*, vol. 53, no. 2, pp. 1028–1037, Mar./Apr. 2017.

[15] X. Liu and Z. Q. Zhu, "Stator/rotor pole combinations and winding configurations of variable flux reluctance machines," *IEEE Trans. Ind. Appl.*, vol. 50, no. 6, pp. 3675–3684, Nov./Dec. 2014.

[16] X. Liu and Z. Q. Zhu, "Electromagnetic performance of novel variable flux reluctance machines with DC-Field coil in stator," *IEEE Trans. Magn.*, vol. 49, no. 6, pp. 3020–3028, Jun. 2013.

[17] S. Jia, R. Qu, J. Li, and D. Li, "Flux modulation principles of DC-biased sinusoidal current vernier reluctance machines," in *Proc. IEEE Energy Convers. Congr. Expo.*, Sep. 2016, pp. 1–8.

[18] S. Jia, R. Qu, D. Li, J. Li, and W. Kong, "Improved torque capacity for flux modulated machines by injecting DC currents into the armature windings," *IEEE Trans. Magn.*, vol. 53, no. 6, Jun. 2017, Art. no. 8102205.

[19] S. Jia, R. Qu, J. Li, D. Li, and R. Zhang, "Stator/rotor slot and winding pole pair combinations of DC biased sinusoidal vernier reluctance machines," in *Proc. Int. Conf. Electr. Mach.*, Sep. 2016, pp. 904–910.

[20] Z. Q. Zhu and B. Lee, "Integrated field and armature current control for dual three-phase variable flux reluctance machine drives," *IEEE Trans. Energy Convers.*, vol. 32, no. 2, pp. 447–457, Jun. 2017.

[21] Z. Q. Zhu, B. Lee, and X. Liu, "Integrated field and armature current,control strategy for variable flux reluctance machine using open winding," *IEEE Trans. Ind. Appl.*, vol. 52, no. 2, pp. 1519–1529, Mar./Apr. 2016.

[22] D. Li, T. Zou, R. Qu, and D. Jiang, "Analysis of fractional-slot concentrated winding PM vernier machines with regular open-slot stators," *IEEE Trans. Ind. Appl.*, vol. 54, no. 2, pp. 1320–1330, Mar./Apr. 2018.

[23] S. Jia, R. Qu, J. Li, D. Li, and W. Kong, "A stator-PM consequent-pole vernier machine with hybrid excitation and DC-biased sinusoidal current," *IEEE Trans. Magn.*, vol. 53, no. 6, pp. 1–4, Jun. 2017.

[24] M. R. Baiju, K. K. Mohapatra, R. S. Kanchan, and K. Gopakumar, "A dual two-level inverter strategy with common mode voltage elimination for an induction motor drive," *IEEE Trans. Power Electron.*, vol. 19, no. 3, pp. 794–805, May 2004.

[25] H. Nian, Y. Zhou, and H. Zeng, "Zero-sequence current suppression strategy for open winding PMSG fed by semicontrolled converter," *IEEE Trans. Power Electron.*, vol. 31, no. 1, pp. 711–720, Jan. 2006.

[26] A. Edpuganti and A. K. Rathore, "New optimal pulsewidth modulation for single dc-link dual-inverter fed open-end stator winding induction motor drive," *IEEE Trans. Power Electron.*, vol. 30, no. 8, pp. 4386–4393, Aug. 2015.

[27] Z. Q. Zhu, B. Lee, L. Huang, and W. Chu, "Contribution of current harmonics to average torque and torque ripple in switched reluctance machines," *IEEE Trans. Magn.*, vol. 53, no. 3, pp. 1–9, Mar. 2017.
[28] Z. Yu, D. Li, W. Kong, R. Qu, S. Jia, D. Jiang, and Y. Zhou, "New optimal current control strategy for six-phase DC-biased vernier reluctance machines considering distorted EMF," *IEEE Trans. Power Electron.*, Feb. 2018.
[29] Z.Q. Zhu, M. Al-Ani, B. Lee, and X. Liu, "Comparative study of the electromagnetic performance of switched flux permanent magnet machines," *IET Electr. Power Appl.*, vol. 9, no. 4, pp. 297–306, 2015.
[30] H. Nian and Y. Song, "Optimised parameter design of proportional integral and resonant current regulator for doubly fed induction generator during grid voltage distortion," *IET Renew. Power Gen.*, vol. 8, no. 3, pp. 299–313, Mar. 2014.
[31] Y. S. Hu, Z. Q. Zhu, and K. Liu, "Current control for dual three-phase permanent magnet synchronous motors accounting for current unbalance and harmonics," *IEEE J. Emerg. Sel. Topics Power Electron.*, vol. 2, no. 2, pp. 272–284, Jun. 2014.

Zixiang Yu (S'16) was born in Liaoning, China, in 1993. He received the B.E.E degree in electrical engineering from Dalian Maritime University, Dalian, China, in 2015. He is currently working toward the M.S. degree with the School of Electronic and Electrical Engineering, Huazhong University of Science and Technology, Wuhan, China.

His current research focuses on control strategy of PM machines, reluctance machines, and multiphase machines.

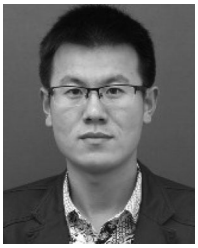

Wubin Kong (M'15) was born in Zhejiang, China, in 1986. He received the B.S. and Ph.D. degrees in electrical engineering from Zhejiang University, Hangzhou, China, in 2009 and 2014, respectively.

From 2015, he has been a Lecturer with Huazhong University of Science and Technology, Wuhan, China. His research interests include high-power multiphase motor drives and fault tolerant control motor drive applied in EV.

Ronghai Qu (S'01–M'02–SM'05–F'18) was born in China. He received the B.E.E. and M.S.E.E. degrees in electrical engineering from Tsinghua University, Beijing, China, in 1993 and 1996, respectively, and the Ph.D. degree in electrical engineering from the University of Wisconsin-Madison, Madison, WI, USA, in 2002.

In 1998, he joined the Wisconsin Electric Machines and Power Electronics Consortiums as a Research Assistant. He became a Senior Electrical Engineer with Northland, a Scott Fetzer Company in 2002. Since 2003, he has been with the General Electric (GE) Global Research Center, Niskayuna, NY, USA, as a Senior Electrical Engineer with the Electrical Machines and Drives Laboratory. He has authored more than 50 published technical papers and is the holder of more than 40 patents/patent applications. Since 2010, he has been a Professor with Huazhong University of Science and Technology, Wuhan, China.

Prof. Qu is a full member of Sigma Xi. He has been the recipient of several awards from GE Global Research Center since 2003, including the Technical Achievement and Management Awards. He is also the recipient of the 2003 and 2005 Best Paper Awards, third prize, from the Electric Machines Committee of the IEEE Industry Applications Society at the 2002 and 2004 IAS Annual Meeting, respectively.

Dawei Li (S'12–M'15) was born in China. He received the B.E.E. degree in electrical engineering from Harbin Institute of Technology, Harbin, China, in 2010, and the Ph.D. degree in electrical engineering from Huazhong University of Science and Technology, Wuhan, China, in 2015.

In July 2015, he joined Huazhong University of Science and Technology. He has authored more than 60 published technical papers and is the holder of more than ten patents/patent applications. His research areas include the design and analysis of flux-modulation permanent-magnet brushless machines.

Dr. Li was the recipient of the Best Poster Presentation Award from the XXIIth International Conference on Electrical Machines, and Hubei Province Excellent Doctoral Dissertation (2016), China.

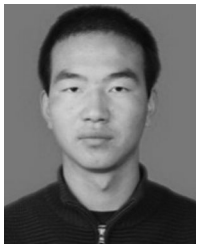

Shaofeng Jia (S'14–M'17) was born in Shaanxi, China. He received the B.Eng. degree in electrical engineering from Xi'an Jiaotong University, Xi'an, China, in 2012, and Ph.D. degree in electrical engineering from Huazhong University of Science and Technology, Wuhan, China, in 2017.

He is currently an Assistant Professor with the School of Electrical Engineering, Xi'an Jiaotong University. His research interests include design and analysis of novel PM and reluctance machines. He is the author/coauthor of 30 IEEE technical papers.

Dong Jiang (S'05–M'12–SM'16) received the B.S. and M.S. degrees in electrical engineering from Tsinghua University, Beijing, China, in 2005 and 2007, respectively. He started working toward the Ph.D. degree with the Center for Power Electronics Systems, Virginia Tech, Blacksburg, VA, USA, in 2007 and was transferred to University of Tennessee with his advisor in 2010. He received the Ph.D. degree in power electronics and motor drives from the University of Tennessee, Knoxville, TN, USA, in December 2011.

He was with United Technologies Research Center, East Hartford, CT, USA, as a Senior Research Scientist/Engineer from January 2012 to July 2015. He has been with Huazhong University of Science and Technology, Wuhan, China, as a Professor since July 2015. His major research area includes power electronics and motor drives, with more than 40 published IEEE journal and conference papers in this area.

Dr. Jiang has two best paper awards in IEEE conferences. He is an Associate Editor of IEEE TRANSACTIONS ON INDUSTRY APPLICATIONS.

Jianbo Sun (M'01) was born in China. He received the B.Eng. and Ph.D. degrees in electrical engineering from Huazhong University of Science and Technology, Wuhan, China, in 2001 and 2005, respectively.

He is currently an Assistant Professor with the School of Electrical and Electronic Engineering, Huazhong University of Science and Technology. His research interests include design and analysis of novel PM machines, reluctance machines, and transformer.

Hongtao Li was born in China. He received the B.S. degree in electrical engineering from China Jiliang University, Hangzhou, China, in 2014, and the M.S. degree in electrical engineering from Hefei University of Technology, Hefei, China, in 2017.

He is currently working at State Grid Zhejiang Electric Power Company Hangzhou Power Supply Company, Hangzhou, China. His research interests include motor drive control of electric vehicle.